

Received February 13, 2022, accepted March 8, 2022, date of publication March 14, 2022, date of current version March 24, 2022.

Digital Object Identifier 10.1109/ACCESS.2022.3159675

# Vibration Mechanism and Compensation Strategy of Magnetic Suspension Rotor System Under Unbalanced Magnetic Pull

LI JI  AND XUEQING MA

School of Information Engineering, Hangzhou Dianzi University, Hangzhou 310018, China

Corresponding author: Li Ji (jili198504@hdu.edu.cn)

This work was supported by the Natural Science Foundation of Jiangsu Province under Grant BK20190491.

**ABSTRACT** The existing imbalance compensation strategies for magnetic suspension motors mainly focus on the mass unbalance force, ignoring the effects of the unbalanced magnet pull (UMP). This paper studied the vibration mechanism and compensation strategy of magnetic suspended permanent magnet synchronous motor (PMSM) under the influence of UMP. Firstly, an analytical model of the flux density was established based on equivalent magnetic circuit method, then the analytical expressions of UMP was deduced by Maxwell stress tensor method. Furthermore, an unbalanced compensation method based on hypothetical reference frame (HRF) transformation was proposed. The stability of the closed-loop system with compensation was analyzed based on the complex-coefficients theory. The proposed model and compensation strategy were verified by the simulations and experiments. The results indicate that the proposed compensation strategy can achieve effective suppression of the magnetic rotor vibration.

**INDEX TERMS** AMB-based motor, vibration compensation, unbalanced magnetic pull, hypothetical reference frame.


## LIST OF PRINCIPAL SYMBOLS

$B$	Magnetic induction intensity.
$F_j$	Permanent magnet MMF.
$F_s$	Armature MMF.
$G$	The coefficient concerning gyroscopic.
$K_P/K_I/K_D$	The three parameters of the PID controller.
$K_i$	Current stiffness of AMBs.
$K_{xy}$	Displacement stiffness of AMBs.
$M$	Equivalent mass of the rotor.
$P_d/P_q$	DC components of the compensations.
$P_x/P_y$	Compensations in Cartesian coordinates.
$d/d_0$	Eccentricity/Static eccentricity.
$f_{ump}$	Unbalanced magnetic pull.
$k_n$	Coefficient of UMP.
$v_x/v_y$	Rotor displacement errors.
$v_d/v_q$	Rotor displacement errors in hypothetical reference frame.
$\alpha$	The relative electrical angle between rotor d-axis and stator A-axis.

$\beta$	The advance supplementary angle.
$\gamma/\gamma_0$	Eccentric angle/Static eccentric angle.
$\delta/\delta_0$	Air gap length/Nominal air gap length.
$\varepsilon$	Relative eccentricity, $\varepsilon = d/\delta_0$ .
$\lambda$	Torque angle, the angle between the MMF of stator and rotor.
$\mu_0$	Vacuum permeability.
$\varphi$	The initial phase difference between the A-axis and the eccentric position.
$\omega_r$	Angular speed of rotor.

## I. INTRODUCTION

The high-speed magnetic suspended motor (the rotor is supported by the magnetic bearing) with high speed (over 10000rpm) can be directly connected to the high speed working machine without acceleration and deceleration devices. In addition, the magnetic bearings eliminate contact, friction and lubrication system between the stator and the rotor, reducing maintenance costs and extending the life of the motor. The use of AMB-based machine to upgrade the conventional equipment (such as fans, compressors and gas turbines) can increase equipment efficiency significantly [1]–[4].

The associate editor coordinating the review of this manuscript and approving it for publication was Christopher H. T. Lee .

Despite their many advantages, magnetic bearings have limited force capacity and imbalance in the rotor mass will cause relatively large synchronous vibration (dynamic eccentricity) when rotor rotates at a high speed [5]. Eccentricity can cause magnetic field distortion, resulting in an unbalanced magnetic pulling force (UMP). In turn, UMP will accelerate the vibration, which may cause instability and collapse of the entire magnetic system. Thus, it is necessary to study the vibration mechanism and compensation strategy of the magnetic suspended rotor under the UMP.

At present, the researches on vibration control of magnetic suspension rotor system mainly focuses on the mass imbalanced force. There are two types of compensation strategies. One strategy is automatic balancing realized mainly through notch filter [6], LMS filter [7], repeated control [8], [9], iterative search [10] and sliding mode interference observer [11]. The purpose of this method is to prevent the susceptor vibration caused by the unbalanced force, but the eccentricity of the rotor may increase, which will result in an increase in the unbalanced magnetic pull. Positive feedback between the unbalanced force and the eccentricity could cause the instability of the magnetic suspension system.

The other compensation strategy is to force the rotor to rotate about its geometric axis for better rotation accuracy. Nonami *et al.* [12] proposed a feedforward unbalanced compensation algorithm based on an iterative approximation, which can realize the identification and suppression of interference signals without the system model. Jiang *et al.* [13] reduced the variable search time for the unbalanced mass independent of the rotational speed by a Fourier iterative search method. Mao *et al.* [14] proposed a variable step size iterative search algorithm to improve the identification speed. Wang *et al.* [15] realized unbalanced compensation control by applying an unbalanced coefficient identification. Shi *et al.* [16] conducted the minimum displacement and minimum current compensation, respectively, based on an adaptive filtering LMS algorithm. Song *et al.* [17] used a variable polarity LMS feedback based on displacement nulling to compensate unbalance of magnetic bearing. Schuhmann *et al.* [18] improved the stiffness and dynamic performance of the magnetic bearings through Kalman filtering and LQG state feedback controller. Han *et al.* [19] applied a repetitive control method to the control system of magnetic bearings, and the vibration of the rotor was effectively reduced.

For the unbalanced compensation strategies, the researches mainly focus on the mass imbalance force. The effects of the UMP have not been systematically studied. In addition, most of the existing compensation methods apply the adaptive iterative algorithm to learn the rotor unbalance parameters. The contradiction between convergence speed and compensation accuracy is inevitable, which results in vibration compensation only for certain rotor speeds. Therefore, it is difficult to realize vibration suppression over the entire rotor speed range. In this paper, an analytical model

of UMP based on the special structure of the AMB-based motor was proposed, and a compensation method based on a hypothetical reference frame (HRF) transformation was developed. Finally, the proposed model and compensation strategy were verified by the simulations and experiments.

## II. MODEL OF THE UNBALANCED MAGNETIC PULL

### A. MODEL OF THE ECCENTRIC MAGNETIC DENSITY

The AMB-based motor has the advantages of high-power density and small size, and it is also a complicated machine that consists of the rotor, magnetic bearing, motor stator, displacement sensor, catcher bearing *et al.* Moreover, there are complicated eccentricity (both static eccentricity and dynamic eccentricity) during operation. The geometric relationship of the rotor eccentricity can be described in the dual coordinate systems, as shown in Figure 1.

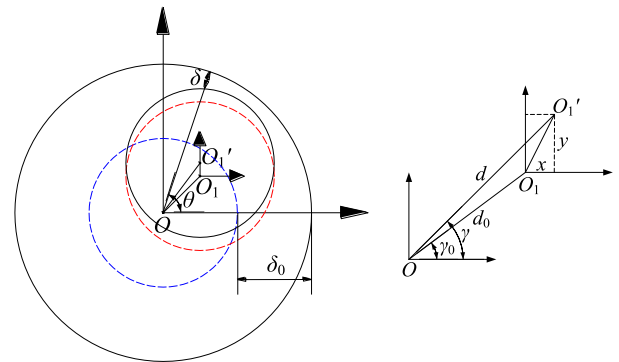


FIGURE 1. Cross-section of the maglev stator-rotor under air-gap eccentricity.

The motor center  $O$  is the origin of the  $d$ - $\gamma$  coordinate, and the magnetic bearing center  $O_1$  is the origin of the  $x$ - $y$  coordinate,  $O'_1$  is the geometric center of the rotor. Where  $\delta_0$  is the nominal air gap length,  $d_0$  and  $\gamma_0$  are the static eccentricity and the eccentric angle;  $d$  and  $\gamma$  is actual eccentricity and eccentric angle of the rotor with both static and dynamic eccentricity.

Since the rotor radius is much larger than the eccentricity, the air gap length at any angle  $\theta$  can be approximated as:

$$\delta(\theta) \approx \delta_0 - d \cos(\theta - \gamma) \quad (1)$$

Both the eccentricity and the eccentric angle in the equation can be expressed as a function of  $x$  and  $y$ .

$$d = \sqrt{(d_0 \cos \gamma_0 + x)^2 + (d_0 \sin \gamma_0 + y)^2} \quad (2)$$

$$\tan \gamma = \frac{d_0 \sin \gamma_0 + y}{d_0 \cos \gamma_0 + x} \quad (3)$$

The permeability at any air gap of motor can be expanded into a Fourier series form [17]:

$$\begin{aligned} \Lambda(\theta) &= \frac{\mu_0 dS}{\delta(\theta)} = \frac{\mu_0 dS}{\delta_0 [1 - \varepsilon \cos(\theta - \gamma)]} \\ &= dS \sum_{n=0}^{\infty} \Lambda_n \cos n(\theta - \gamma) \end{aligned} \quad (4)$$

where  $dS$  is the magnetic pole area corresponding to the unit angle  $\theta$ ,  $\varepsilon$  is the relative eccentricity, and  $\varepsilon = d/\delta_0$ . The coefficient of  $\Lambda_n$  is shown in formula (5).

$$\Lambda_n = \begin{cases} \frac{\mu_0}{\delta_0 \sqrt{1-\varepsilon^2}} & (n=0) \\ \frac{2\mu_0}{\delta_0 \sqrt{1-\varepsilon^2}} \left( \frac{1-\sqrt{1-\varepsilon^2}}{\varepsilon} \right)^n & (n>0) \end{cases} \quad (5)$$

According to the principle of the permanent magnet motor, the magneto motive force (MMF) is composed of the permanent magnet  $F_j$  and Armature  $F_s$ . Therefore the resultant MMF in the air gap can be expressed as:

$$\begin{aligned} F(\theta) &= F_j(\theta) + F_s(\theta) \\ &= F_{j0} \cos(\alpha - p\theta) + F_{s0} \cos(\alpha - p\theta - \lambda) \end{aligned} \quad (6)$$

where  $p$  is the rotor pole pair number;  $F_{j0}$  and  $F_{s0}$  represent the MMF fundamental wave amplitudes of stator and rotor;  $\alpha$  is the relative electrical angle between rotor d-axis and stator A-axis.  $\lambda$  is the angle between the MMF of stator and rotor (torque angle), which is related to the control strategy of motor.

Ignoring the reluctance of ferromagnetic materials, the expression of the magnetic induction intensity of the air gap with any angle  $\theta$  is:

$$\begin{aligned} B(\theta) &= \frac{\Lambda(\theta) \cdot F(\theta)}{S} \\ &= F(\theta) \cdot \sum_{n=0}^{\infty} \Lambda_n \cos n(\theta - \gamma) \end{aligned} \quad (7)$$

## B. ANALYTICAL MODEL OF UNBALANCED MAGNETIC PULL

In the case of one pole pair, the radial UMP acting on the rotor due to eccentricity can be obtained based on the Maxwell stress tensor.

$$\left\{ \begin{aligned} f_{ump\_x} &= \frac{LR\pi}{8\mu_0} [k_1 \cos \gamma + k_2 \cos(\gamma + \lambda) \\ &\quad + k_3 \cos(\gamma - \lambda) + k_4 \cos(2\alpha - \gamma) \\ &\quad + k_5 \cos(3\gamma - 2\alpha) + k_6 \cos(2\alpha - \gamma - \lambda) \\ &\quad + k_7 \cos(2\alpha - \gamma - 2\lambda) + k_8 \cos(3\gamma - 2\alpha + 2\lambda) \\ &\quad + k_9 \cos(3\gamma - 2\alpha + \lambda)] \\ f_{ump\_y} &= \frac{LR\pi}{8\mu_0} [k_1 \sin \gamma + k_2 \sin(\gamma + \lambda) \\ &\quad + k_3 \sin(\gamma - \lambda) + k_4 \sin(2\alpha - \gamma) \\ &\quad + k_5 \sin(3\gamma - 2\alpha) + k_6 \sin(2\alpha - \gamma - \lambda) \\ &\quad + k_7 \sin(2\alpha - \gamma - 2\lambda) + k_8 \sin(3\gamma - 2\alpha + 2\lambda) \\ &\quad + k_9 \sin(3\gamma - 2\alpha + \lambda)] \end{aligned} \right. \quad (8)$$

where  $\mu_0$  is the vacuum permeability and  $k_n$  is the coefficient of UMP.

$$\begin{aligned} k_1 &= 4F_{j0}^2 \Lambda_0 \Lambda_1 + 2F_{j0}^2 \Lambda_1 \Lambda_2 + 2F_{j0}^2 \Lambda_2 \Lambda_3 + 4F_{s0}^2 \Lambda_0 \Lambda_1 \\ &\quad + 2F_{s0}^2 \Lambda_1 \Lambda_2 + 2F_{s0}^2 \Lambda_2 \Lambda_3 \\ k_2 &= 4F_{j0} F_{s0} \Lambda_0 \Lambda_1 + 2F_{j0} F_{s0} \Lambda_1 \Lambda_2 + 2F_{j0} F_{s0} \Lambda_2 \Lambda_3 \end{aligned}$$

$$\begin{aligned} k_3 &= 4F_{j0} F_{s0} \Lambda_0 \Lambda_1 + 2F_{j0} F_{s0} \Lambda_1 \Lambda_2 + 2F_{j0} F_{s0} \Lambda_2 \Lambda_3 \\ k_4 &= 2F_{j0}^2 \Lambda_0 \Lambda_1 + F_{j0}^2 \Lambda_1 \Lambda_2 + F_{j0}^2 \Lambda_2 \Lambda_3 \\ k_5 &= 2F_{j0}^2 \Lambda_0 \Lambda_3 + F_{j0}^2 \Lambda_1 \Lambda_2 \\ k_6 &= 4F_{j0} F_{s0} \Lambda_0 \Lambda_1 + 2F_{j0} F_{s0} \Lambda_1 \Lambda_2 + 2F_{j0} F_{s0} \Lambda_2 \Lambda_3 \\ k_7 &= 2F_{s0}^2 \Lambda_0 \Lambda_1 + F_{s0}^2 \Lambda_1 \Lambda_2 + F_{s0}^2 \Lambda_2 \Lambda_3 \\ k_8 &= 2F_{s0}^2 \Lambda_0 \Lambda_3 + F_{s0}^2 \Lambda_1 \Lambda_2 \\ k_9 &= 4F_{j0} F_{s0} \Lambda_0 \Lambda_3 + 2F_{j0} F_{s0} \Lambda_1 \Lambda_2 \end{aligned} \quad (9)$$

Obviously, the analytical expression of UMP is very complicated. It includes three fixed-direction force vectors, three double frequency positive sequence components and three double frequency negative sequence components. In order to simplify the formula (8), the magnitude of each component is analyzed under different eccentricity  $\varepsilon$  (%) and load rates (%), and the curves obtained are shown in Figure 2.

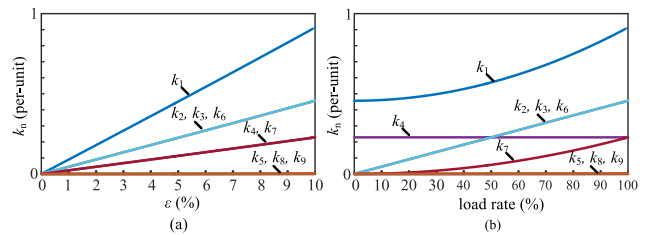


**FIGURE 2. Unbalanced magnetic pull coefficient against eccentricity and load rate. (a) Coefficient curves for various eccentricity. (b) Coefficient curves for various load rate.**

As shown in the above figure, the amplitudes of the coefficients  $k_5$ ,  $k_8$ , and  $k_9$  within the entire load range and 10% relative eccentricity are extremely small. Therefore, 5<sup>th</sup>, 8<sup>th</sup>, and 9<sup>th</sup> items in formula (8) are negligible. The coefficients of the 2nd and 3rd items are the same and the phase is symmetric about  $\gamma$ . Thus, they can be merged into one force vector with the first items which is in the same direction as the eccentricity. The 4<sup>th</sup>, 6<sup>th</sup>, and 7<sup>th</sup> items are related to the initial angle  $\varphi$ . Where,  $\varphi$  represents the initial phase difference between the A-axis and the eccentric position.

Moreover, in AMB-based motor, the eccentric angle of the rotor is synchronous with the rotational speed. Therefore, let  $\alpha = \omega_r t$ ;  $\gamma = \omega_r t + \varphi$ . And bring them into formula (8), it can be found that all the items of the UMP in the steady state are positive sequence components with the same frequency as the rotate speed. Therefore, the total UMP exhibits a synchronous rotational force vector, and its amplitude and phase depend on many factors such as the eccentricity  $\varepsilon$ , the torque angle  $\lambda$ , and the initial phase difference  $\varphi$ .

## C. CHARACTERISTIC ANALYSIS OF UMP

According to the above calculated results, the unbalanced electromagnetic pull of the AMB-based motor at no load is analyzed, as shown in Fig 3. Fig 3(a) and (b) show the force on the rotor when static eccentricity is ignored and the dynamic eccentricity amplitude is 0.1mm. Four curves correspond to four different initial dynamic eccentricity angles. 1-4 correspond to the initial dynamic eccentricity angles  $\varphi = 0^\circ$ ,

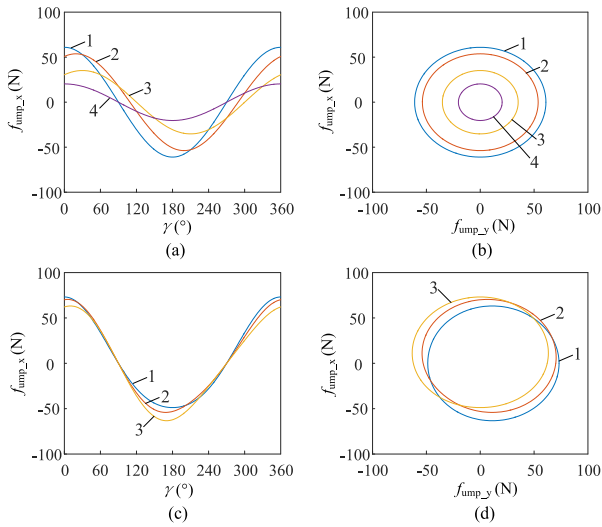


**FIGURE 3. The waveforms of unbalanced magnetic pull during no-load. (a)  $f_{ump-x}$  curves with eccentric angle  $\gamma$  for various initial phase difference  $\varphi$ . (b) Vector diagram of  $f_{ump}$  with dynamic eccentricity. (c)  $f_{ump-x}$  curves with eccentric angle  $\gamma$  for various static eccentric angle  $\gamma_0$ . (d) Vector diagram of  $f_{ump}$  with both static eccentricity and dynamic eccentricity.**

30°, 60°, 90° respectively, and their amplitudes are: 60.0N, 54.7N, 35.2N, 20.3N respectively. It can be seen that in the case of no load, the unbalanced magnetic pull of the rotor depends not only on the eccentricity, but also on the angle between the eccentricity displacement and the position of the rotor magnetomotive force. Under the same dynamic eccentricity, if the position of the rotor magnetomotive force is the same as the eccentricity position ( $\varphi = 0^\circ$ ), the rotor is subjected to the maximum unbalanced magnetic pull, and the phase of the pull is the same as the rotor dynamic unbalance phase. If the phase of the rotor magnetomotive force is different from the eccentric phase, the amplitude of the unbalanced pull decreases and the phase shifts. When the direction of the rotor magnetomotive force is perpendicular to the eccentric direction ( $\varphi = 90^\circ$ ), the amplitude of the unbalanced pull is minimum. If the unbalanced pull in the x and y directions is combined into vector form, as shown in Fig. 3(b), it can be seen that the trajectory of the vector of the unbalanced pull is circular with only dynamic eccentricity, and the amplitude of the unbalanced pull in the x and y directions is always the same. The difference between the direction of rotor magnetic field and the eccentric direction only affects the amplitude and phase of the unbalanced pull, but does not distort the trajectory of the resultant force.

Fig. 3(c) and (d) show the rotor subjected to unbalanced pull when static eccentricity (amplitude: 0.02mm) and dynamic eccentricity (amplitude: 0.1mm) are considered simultaneously. Curves 1-3 in Fig. 3(c) correspond to static eccentricity angles  $\gamma_0 = 0^\circ, 45^\circ$  and  $90^\circ$  respectively. In order to verify the effect of static eccentricity, the initial dynamic eccentricity angle  $\varphi = 0^\circ$  is set. It can be seen that when  $\gamma_0$  changes, the magnitude of the pull doesn't change much, but there is a DC component in the waveform. As shown in Figure 4(c), the mean values of curves 1-3 are 6.25N, 4.5N and  $3 \times 10.15$ N respectively. It can be seen that when the

static eccentricity is all in the x direction, the  $F_x$  offset is the largest. When the static eccentricity is completely located in the y direction, the x direction is not affected, and positive and negative semicircles are symmetric. The y direction is the opposite. It can be concluded that the static eccentricity will cause the unbalanced pull of the rotor to be offset in the same direction as the static eccentricity.

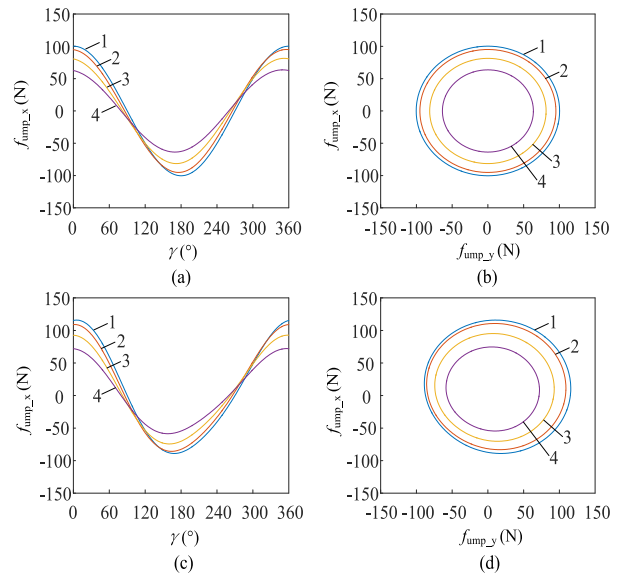


**FIGURE 4. The waveforms of unbalanced magnetic pull during full-load. (a)  $f_{ump-x}$  curves with eccentric angle  $\gamma$  for various torque angle  $\lambda$ . (b) Vector diagram of  $f_{ump}$  with dynamic eccentricity. (c)  $f_{ump-x}$  curves with eccentric angle  $\gamma$  for various torque angle  $\lambda$  involve static eccentricity. (d) Vector diagram of  $f_{ump}$  with both static eccentricity and dynamic eccentricity.**

The force of magnetic levitation rotor under load is shown in Fig. 4. Fig. 4(a) and (b) show the rotor subjected to unbalanced pull when only dynamic eccentricity (0.1mm) is considered and the initial phase angle  $\varphi = 0^\circ$ . Considering the influence of different motor control strategies, the stator and rotor torque angles are different. In this paper, four cases are calculated. Curves 1-4 in Figure 4(a) represent the unbalanced pull of the rotor in the x direction when the rotor torque angle  $\lambda$  is  $0^\circ, 30^\circ, 60^\circ$  and  $90^\circ$ , with amplitude of 100.3N, 95.1N, 81.4N and 63.6N respectively. It can be seen that although the amplitudes of the stator and rotor magnetomotive forces in curve 4 are the same, the difference in torque angle affects both the amplitude and phase of the unbalanced pull. When the torque angle is zero, the unbalanced pull amplitude of the rotor is the largest, but with the increase of the torque angle, the unbalanced pull of the rotor is gradually reduced, and the phase changes. When the torque angle is  $90^\circ$ , the rotor suffers the least unbalanced pull.

Fig. 4(c) and (d) show the unbalanced pull when static eccentricity (amplitude 0.02mm, static eccentricity angle  $\gamma_0 = 45^\circ$ ) and dynamic eccentricity (amplitude 0.1mm) are considered simultaneously. The definitions of curves 1-4 in Fig. 4(c)(d) are the same as those in Fig 4(a)(b). It can be seen that, first of all, the unbalanced pull of the rotor is offset along the positive direction of the x and y axes, and its amplitude changes in the same way as (a) and (b). The maximum tension

is achieved when the torque angle is zero, and the minimum tension is achieved when the torque angle is 90°.

### III. UNBALANCED COMPENSATION STRATEGY

#### A. CONTROL STRUCTURE OF THE PROPOSED COMPENSATOR

According to the above analysis and results, it can be seen that eccentricity can cause considerable vibration on the magnetic suspension rotor, so the strategies of automatic balancing could result in an increase in vibration. The essence of this paper is to estimate the unbalanced force, reverse and add to the control current, used to offset the unbalanced force. Based on previous researches [20]–[22], an HRF-based imbalance compensation controller is proposed. The structure used in feedforward compensation is shown in Fig. 5, where  $H(s)$ ,  $C(s)$ ,  $A(s)$ ,  $R(s)$  and  $K_s$  are compensator, master controller, power amplifier, magnetic suspension bearing-rotor and displacement sensor, respectively. The compensator is connected in parallel with the original system controller, and the gain  $\varepsilon$  is used to accelerate convergence. Taking the detected displacement error as input, the control quantity of the compensator is added to the output of the original controller.

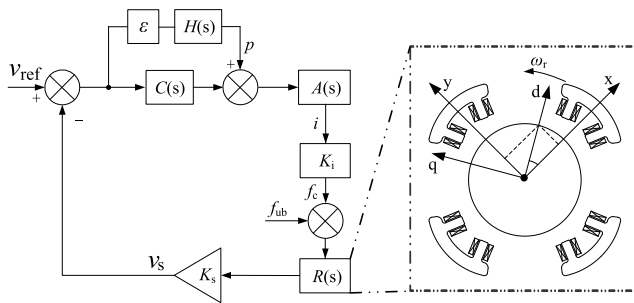


FIGURE 5. The feedforward compensation control system of the magnetic bearing.

The compensator determines the displacements according to the hypothetical reference frame d-q axis, which rotates synchronously with the actual rotor. Figure 5 shows a cross-sectional view of the rotor, which defines two orthogonal coordinate systems (the x-y and d-q axis).

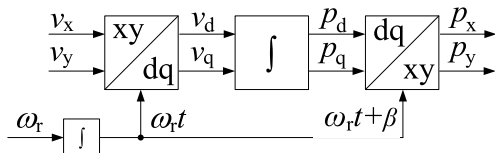


FIGURE 6. Structure diagram of HRF compensator.

Fig. 6 shows the internal structure of the compensator, which mainly consists of a coordinate transformation module and an integrator. The principle of the compensator is as follows: two orthogonal rotor displacement errors  $v_x$  and  $v_y$  are converted into DC signals ( $v_d$ ,  $v_q$ ), and in the ideal case, there is no harmonic component in the DC signal. However, due to the difference in each control loop, the obtained DC signal still has a certain amount of harmonic interference. To further improve the control performance,

an integrator is introduced to eliminate the harmonic and amplify synchronous signal. Finally, the control quantities are converted into an AC control signal with a phase shifting through inverse transformation and superimposed into the output of the original controller.

#### B. MECHANISM OF HYPOTHETICAL REFERENCE FRAME

The HRF transformation matrix  $T(\omega_r t)$  can be expressed as:

$$T(\omega_r t) = \begin{bmatrix} \cos(\omega_r t) & \sin(\omega_r t) \\ -\sin(\omega_r t) & \cos(\omega_r t) \end{bmatrix} \quad (10)$$

The two orthogonal signals  $[v_x, v_y]$  can be expressed as  $[A_0 \cos(\omega_r t + \varphi), A_0 \sin(\omega_r t + \varphi)]$ , and after coordinate transformation, one can obtain:

$$\begin{bmatrix} v_d \\ v_q \end{bmatrix} = \begin{bmatrix} \cos(\omega_r t) & \sin(\omega_r t) \\ -\sin(\omega_r t) & \cos(\omega_r t) \end{bmatrix} \begin{bmatrix} A_0 \cos(\omega_r t + \varphi) \\ A_0 \sin(\omega_r t + \varphi) \end{bmatrix} \\ = \begin{bmatrix} A_0 \cos \varphi \\ A_0 \sin \varphi \end{bmatrix} \quad (11)$$

If the orthogonal signal contains harmonic components  $[A_n \cos(n\omega_r t + n\varphi), A_n \sin(n\omega_r t + n\varphi)]$ , then after transformation, the signal is transformed as:

$$\begin{bmatrix} v_{dn} \\ v_{qn} \end{bmatrix} = \begin{bmatrix} \cos(\omega_r t) & \sin(\omega_r t) \\ -\sin(\omega_r t) & \cos(\omega_r t) \end{bmatrix} \begin{bmatrix} A_n \cos(n\omega_r t + n\varphi) \\ A_n \sin(n\omega_r t + n\varphi) \end{bmatrix} \\ = \begin{bmatrix} A_n \cos(n\omega_r t - \omega_r t + n\varphi) \\ A_n \sin(n\omega_r t - \omega_r t + n\varphi) \end{bmatrix} \quad (12)$$

The corresponding  $n-1$  harmonic component can be obtained, where  $n$  represents the harmonic number. These harmonic components can be eliminated by an integrator. Moreover, the integrator has an infinite gain for the DC component.  $P$  is the gain when the system reaches steady state and can be expressed as:

$$\begin{bmatrix} p_d \\ p_q \end{bmatrix} = \begin{bmatrix} PA_0 \cos \varphi \\ PA_0 \sin \varphi \end{bmatrix} \quad (13)$$

The inverse transformation matrix  $T_{inv}(\omega_r t)$  is expressed as:

$$T_{inv}(\omega_r t) = \begin{bmatrix} \cos(\omega_r t + \beta) & -\sin(\omega_r t + \beta) \\ \sin(\omega_r t + \beta) & \cos(\omega_r t + \beta) \end{bmatrix} \quad (14)$$

where,  $\beta$  is the advance supplementary angle, which is used to improve the stability of the system.

After the inverse synchronous rotation transformation, one can have:

$$\begin{bmatrix} p_x \\ p_y \end{bmatrix} = \begin{bmatrix} \cos(\omega_r t + \beta) & -\sin(\omega_r t + \beta) \\ \sin(\omega_r t + \beta) & \cos(\omega_r t + \beta) \end{bmatrix} \begin{bmatrix} PA_0 \cos \varphi \\ PA_0 \sin \varphi \end{bmatrix} \\ = \begin{bmatrix} PA_0 \cos(\omega_r t + \varphi + \beta) \\ PA_0 \sin(\omega_r t + \varphi + \beta) \end{bmatrix} \quad (15)$$

#### C. STABILITY ANALYSIS OF CONTROL SYSTEM

The proposed HRF compensator uses centralized control for the x and y direction. Therefore, this paper introduces the definition of a complex transfer-function, which helps to build a single-input single-output model from the dual-input dual-output system. Then the classical stability criterion can be used in the proposed system.

The HRF compensator with a phase shift in the continuous time domain is shown in Fig. 6. These sinusoidal signals are internally generated by the sine and cosine blocks. The output signals of the compensator can be described as follow:

$$\begin{aligned}
 p_x(t) &= \cos(\omega_r t + \beta) \int \cos(\omega_r t) v_x(t) dt + \cos(\omega_r t + \beta) \\
 &\quad \times \int \sin(\omega_r t) v_y(t) dt + \sin(\omega_r t + \beta) \\
 &\quad \times \int \sin(\omega_r t) v_x(t) dt - \sin(\omega_r t + \beta) \\
 &\quad \times \int \cos(\omega_r t) v_y(t) dt \quad (16a)
 \end{aligned}$$

$$\begin{aligned}
 p_y(t) &= \sin(\omega_r t + \beta) \int \cos(\omega_r t) v_x(t) dt + \sin(\omega_r t + \beta) \\
 &\quad \times \int \sin(\omega_r t) v_y(t) dt - \cos(\omega_r t + \beta) \\
 &\quad \times \int \sin(\omega_r t) v_x(t) dt + \cos(\omega_r t + \beta) \\
 &\quad \times \int \cos(\omega_r t) v_y(t) dt \quad (16b)
 \end{aligned}$$

After differentiating the above equations, we can obtain the differential equations of the compensator as.

$$\begin{aligned}
 \ddot{p}_x(t) &= -\omega_r^2 p_x(t) - \sin \beta \dot{v}_y(t) + \cos \beta \dot{v}_x(t) \\
 &\quad - \omega_r \sin \beta v_x(t) - \omega_r \cos \beta v_y(t) \quad (17a)
 \end{aligned}$$

$$\begin{aligned}
 \ddot{p}_y(t) &= -\omega_r^2 p_y(t) + \cos \beta \dot{v}_y(t) + \sin \beta \dot{v}_x(t) \\
 &\quad + \omega_r \cos \beta v_x(t) - \omega_r \sin \beta v_y(t) \quad (17b)
 \end{aligned}$$

Then, the transfer function from  $v(s)$  to  $p(s)$  can be derived by Laplace transform, that is

$$\begin{aligned}
 p_x(s) &= \left[ \frac{s \cos \beta}{s^2 + \omega_r^2} - \frac{\omega_r \sin \beta}{s^2 + \omega_r^2} \right] v_x(s) \\
 &\quad - \left[ \frac{s \sin \beta}{s^2 + \omega_r^2} + \frac{\omega_r \cos \beta}{s^2 + \omega_r^2} \right] v_y(s) \quad (18a)
 \end{aligned}$$

$$\begin{aligned}
 p_y(s) &= \left[ \frac{s \cos \beta}{s^2 + \omega_r^2} - \frac{\omega_r \sin \beta}{s^2 + \omega_r^2} \right] v_y(s) \\
 &\quad + \left[ \frac{s \sin \beta}{s^2 + \omega_r^2} + \frac{\omega_r \cos \beta}{s^2 + \omega_r^2} \right] v_x(s) \quad (18b)
 \end{aligned}$$

Multiplying the second equation by  $j$  and adding to the first equation, the complex transfer function  $H(s)$  can be obtained as follows:

$$\begin{aligned}
 H(s) = \frac{(p_x + jp_y)}{(v_x + jv_y)} &= \left[ \frac{s \cos \beta}{s^2 + \omega_r^2} - \frac{\omega_r \sin \beta}{s^2 + \omega_r^2} \right] \\
 &\quad + j \left[ \frac{s \sin \beta}{s^2 + \omega_r^2} + \frac{\omega_r \cos \beta}{s^2 + \omega_r^2} \right] \quad (19)
 \end{aligned}$$

In the same way, the complex transfer function of a magnetic suspension bearing-rotor system considered with a gyroscopic coupling effect can be obtained.

$$R(s) = \frac{(x + yj)}{(i_x + iy_j)} = \frac{K_i}{Ms^2 - K_{xy} - j\omega_r Gs} \quad (20)$$

where,  $M$  is equivalent mass of the rotor,  $G$  is a coefficient concerning gyroscopic,  $K_{xy}$  is displacement stiffness and  $K_i$  is current stiffness.

According to Fig. 5, the characteristic equation of the closed loop system can be expressed as:

$$1 + (C(s) + H(s))A(s)R(s)k_s = 0 \quad (21)$$

$C(s)$  is a classical PID controller,

$$C(s) = K_P + \frac{K_I}{s} + \frac{K_D s}{T_s + 1} \quad (22)$$

where,  $K_P$ ,  $K_I$ , and  $K_D$  are the three parameters of the PID controller, and  $T$  is the time constant of the incomplete differential link.

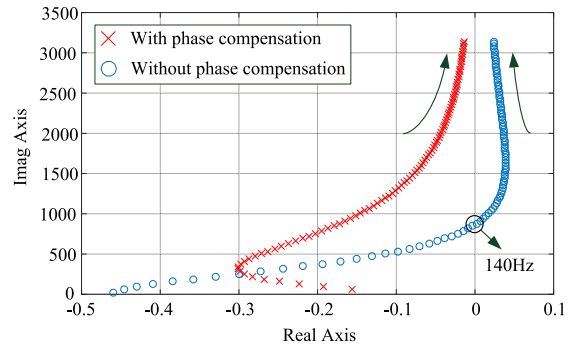


FIGURE 7. Dominant root locus of the control system with HRF compensator in simulation.

$A(s)$  is simplified as a gain. Then, the root locus of a magnetic bearing-rotor system with HRF compensator is shown in Fig. 7, where the frequency varies between 0 to 500Hz. As previously described, the compensation phase  $\beta$  plays an important role in the proposed control method for a stable closed-loop system.

The blue circles with  $\beta = 0$  indicate that the closed-loop root locus are first moved to the right-half plane at a frequency of 140 Hz. This means that the system is unstable when the rotation frequency is above 140 Hz with  $\beta = 0$ . The red star line with  $\beta = \pi/3$  shows that the closed-loop root locus is always located at left-half plane, which means the system with the HRF compensator is stable over the entire frequency.

#### IV. EXPERIMENTAL RESULTS

In this section, experiments are carried out to verify the previous analysis. The experiments were done with a TMS320F28335 digital controller on a 100kW prototype of magnetic suspended permanent magnet motor, as shown in Fig. 8. The detail parameters of the prototype and its controller are shown in Table 1.

First, a steady-state experiment was carried out, and the proposed compensation strategy was applied to four radial controllers. The displacement signal waveforms are shown in Fig. 9, where channels 1-4 of the oscilloscope correspond to the four radial DOFs of the rotor, respectively. It can be seen that the compensation strategy does not affect the stability at steady-state.

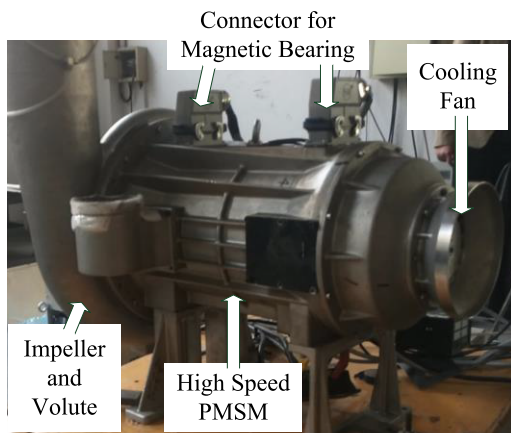


FIGURE 8. Functional prototype of the magnetic suspended PMSM.

TABLE 1. Parameters of the prototype.

Parameters	Value
Rotor quality	12.5 kg
Rotor equatorial inertial moment	0.2526 kg·m <sup>2</sup>
Rotor polar inertial moment	0.0096 kg·m <sup>2</sup>
air gap length	5 mm
Stator effective length	136 mm
Rotor diameter	56 mm
Displacement stiffness	2.34×10 <sup>6</sup> N/m
Current stiffness	380 N/A
Gain of the power amplifier	0.4 A/V
Gain of the displacement sensor	20000 V/m
Parameters PID controller (K <sub>p</sub> , K <sub>i</sub> , K <sub>d</sub> )	3.5, 1.2, 6.5×10 <sup>-3</sup>

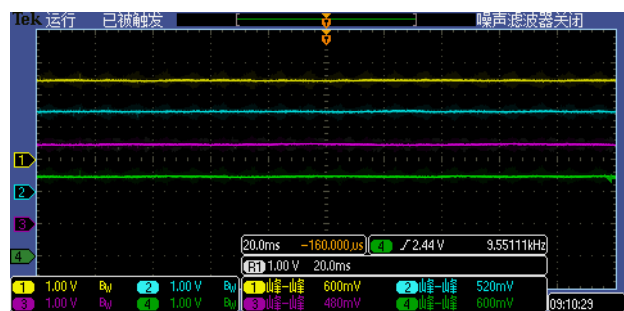


FIGURE 9. Experimental results of control system in steady state with the proposed method.

Then, a speed-up test was carried out to verify the dynamic performance of the proposed control system. In order to obtain an appropriate compensation phase  $\alpha$ , the closed-loop spectrum characteristics of the magnetic bearing-rotor system from the unbalanced force to the output displacement are obtained by frequency sweep analysis, as shown in Fig. 10.

In order to evaluate the performance of the proposed method, a comparison experiment between the HRF compensator and the notch filter was introduced. When the

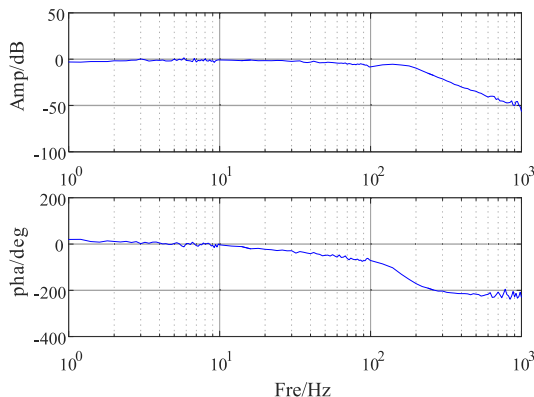


FIGURE 10. Closed-loop spectrum characteristics of the magnetic bearing-rotor system.

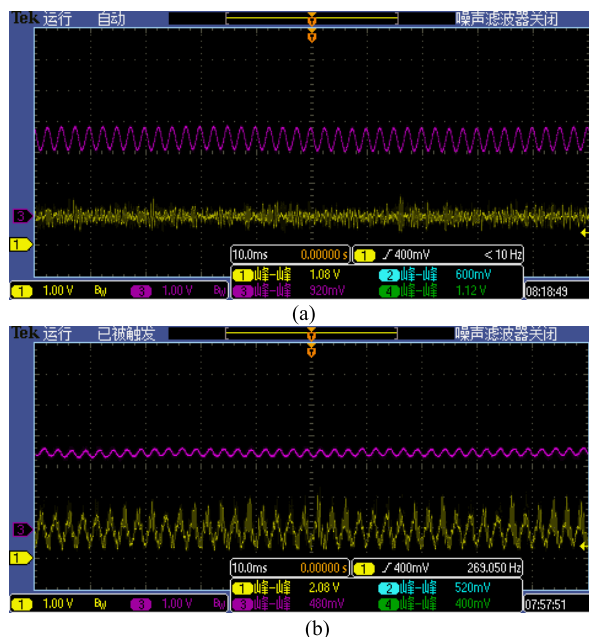


FIGURE 11. Experimental results of magnetic bearing-rotor system with the compensator: (a) adaptive notch filter; (b) HRF compensator.

rated speed is 24000r/min (400Hz), the self-balancing control (notch filter) is applied, and the waveform is shown in Fig. 11 (a). Channels 1 and 3 of the oscilloscope were used to measure the radial control current (the yellow one) and its radial displacement signal (the magenta one). It can be seen from Fig. 13 that at this speed, the rotor can be stably suspended with a vibration peak of 460mV. The corresponding displacement sensor has a sensitivity of 60m/V and a vibration amplitude of 27.6 $\mu$ m. Since the notch filter can suppress the same frequency signal, there is substantially no same frequency component in the corresponding control current. Applying the proposed HRF compensation strategy under the above condition, the displacement vibration waveform of the rotor at 400Hz is shown in Fig. 11 (b). It is worth noting that, compared with the above method, the HRF compensation strategy increases the supporting stiffness of the synchronous frequency signal, and the amplitude of the rotor vibration is significantly

decreased by about 14.4 microns, which is only about 52% of the notch filter control.

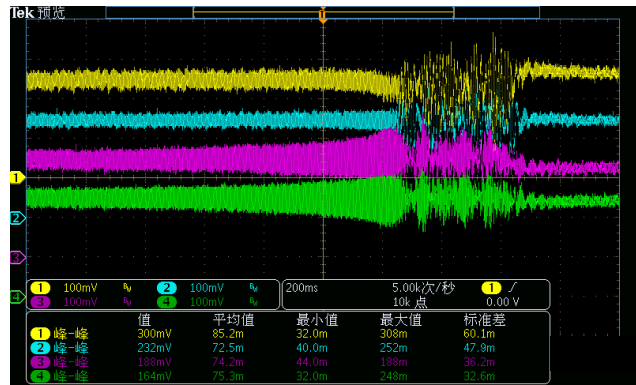


FIGURE 12. Experimental results of magnetic bearing-rotor system without compensation phase  $\beta$ .

In above section, we realized the compensation phase  $\beta$  is very important for the stability of the control system. In the following test, we removed this compensation phase during the speed of 24000r/min, the waveforms of 4 vibration signals are shown in Fig. 12, where channels 1-4 correspond to the four radial DOFs of the rotor respectively. It can be seen that, when the compensation phase is canceled, the eccentricity of rotor gradually increased and eventually collapsed, that is to say, the stability of the bearing-rotor system was definitely influenced by the compensation phase  $\beta$ .

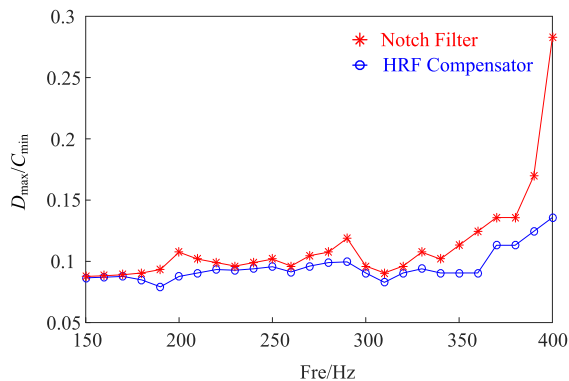


FIGURE 13. Vibration of the magnetic bearing-rotor system under different rotation speed.

According to the evaluation index  $D_{max}/C_{min}$  [23] of the vibration level of the magnetic suspension bearing-rotor system defined by ISO 14839-2, the effects of the above two compensation strategies are compared in different working speed ranges, as shown in Fig. 13. Since the two strategies are very close at low rotation speeds, the vibration of a magnetic bearing at a rotation speed of 150Hz-400Hz is captured. It can be seen that the proposed compensation strategy is more effective in suppressing the rotor vibration.

## V. CONCLUSION

This paper focused on the high speed magnetic suspension permanent magnet motors. Based on the subdomain method,

perturbation method and Maxwell stress tensor method, an analytical model of the unbalanced magnetic pull was established. An unbalanced compensation strategy based on a HRF transformation was developed. The following conclusions can be drawn:

- 1) Based on the special structure of the high speed magnetic suspension permanent magnet motor, the equivalent magnetic circuit method and Maxwell stress tensor method was used to establish a complete analytical model of the biased air gap magnetic field and unbalanced magnetic pull.
- 2) The mathematical model and finite element simulation show that the dynamic eccentricity plays an important role in the magnetic suspension motor system. The unbalanced magnetic pull of the permanent magnet rotor can be represented as a rotating force vector with the same frequency as the rotation speed. There is a linear relationship between the unbalanced magnetic pull and the eccentricity in a small range, and its phase depends on the initial eccentric angle.
- 3) The compensation phase  $\beta$  is very important for the proposed compensation strategy. By selecting an appropriate compensation phase, the closed-loop system with HRF compensator can remain stable over the entire frequency.
- 4) The compensation strategy proposed in this paper does not require complex iterative operation and can suppress the same frequency vibration of the rotor. Compared with the traditional notch filter method, the proposed method has better control effect.

## REFERENCES

- [1] C. Di, I. Petrov, J. J. Pyrhonen, and X. Bao, "Unbalanced magnetic pull compensation with active magnetic bearings in a 2 MW high-speed induction machine by FEM," *IEEE Trans. Magn.*, vol. 54, no. 8, pp. 1-13, Aug. 2018.
- [2] T. Matsuzaki, M. Takemoto, S. Ogasawara, S. Ota, K. Oi, and D. Matsuhashi, "Novel structure of three-axis active-control-type magnetic bearing for reducing rotor iron loss," *IEEE Trans. Magn.*, vol. 52, no. 7, pp. 1-4, Jul. 2016.
- [3] L. Ji, "Vibration mechanism analysis of magnetic levitation rotor system for low temperature waste heat power generation," *Electr. Mach. Control*, vol. 23, no. 11, pp. 67-75, Nov. 2019.
- [4] Y. Xu, J. Zhou, and C. Jin, "Identification of dynamic stiffness and damping in active magnetic bearings using transfer functions of electrical control system," *J. Mech. Sci. Technol.*, vol. 33, no. 2, pp. 571-577, Feb. 2019.
- [5] H. Gao and L. Xu, "Real-time feed-forward force compensation for active magnetic bearings system based on  $H_\infty$  controller," *Chin. J. Mech. Eng.*, vol. 24, no. 1, pp. 58-66, Jan. 2011.
- [6] Q. Chen, G. Liu, and B. Han, "Unbalance vibration suppression for AMBs system using adaptive notch filter," *Mech. Syst. Signal Process.*, vol. 93, pp. 136-150, Sep. 2017.
- [7] M. Dasharatha, B. R. Naik, and N. S. S. Reddy, "Low power and area efficient FIR filter using adaptive LMS algorithm," in *Proc. Int. Conf. Commun. Signal Process. (ICCCSP)*, Chennai, India, Apr. 2017, pp. 0453-0456.
- [8] C. Peng, J. Sun, X. Song, and J. Fang, "Frequency-varying current harmonics for active magnetic bearing via multiple resonant controllers," *IEEE Trans. Ind. Electron.*, vol. 64, no. 1, pp. 517-526, Jan. 2017.
- [9] P. Cui, D. Han, G. Zhang, Z. Liu, and B. Han, "Robust odd repetitive controller for magnetically suspended rotor system," *IEEE Trans. Ind. Electron.*, vol. 66, no. 3, pp. 2025-2033, Mar. 2019.



- [10] Z. Wang, C. Mao, and C. Zhu, "Current compensation control of multiple frequency vibrations of the rotor in active magnetic bearing high speed motors," *Proc. CSEE*, vol. 38, no. 1, pp. 275–284, 2018.
- [11] C. Liu and G. Liu, "Autobalancing control for MSCMG based on sliding-mode observer and adaptive compensation," *IEEE Trans. Ind. Electron.*, vol. 63, no. 7, pp. 4346–4356, Jul. 2016.
- [12] K. Nonami, F. Qi-Fu, and H. Ueyama, "Unbalance vibration control of magnetic bearing systems using adaptive algorithm with disturbance frequency estimation," *JSME Int. J. C Mech. Syst., Mach. Elements Manuf.*, vol. 41, no. 2, pp. 220–226, 1998.
- [13] J. Kejian, Z. Changsheng, and C. Liangliang, "Unbalance compensation by recursive seeking unbalance mass position in active magnetic bearing-rotor system," *IEEE Trans. Ind. Electron.*, vol. 62, no. 9, pp. 5655–5664, Sep. 2015.
- [14] M. Chuan and Z. Changsheng, "Unbalance compensation for active magnetic bearing rotor system using a variable step size real-time iterative seeking algorithm," *IEEE Trans. Ind. Electron.*, vol. 65, no. 5, pp. 4177–4186, May 2018.
- [15] Z. Wang, C. Zhu, and L. Chen, "Parameter design and analysis for two-degrees of freedom radial hybrid magnetic bearings," *China Mech. Eng.*, vol. 38, no. 12, pp. 3699–3708, Jun. 2018.
- [16] J. Shi, R. Zmood, and L. Qin, "Synchronous disturbance attenuation in magnetic bearing systems using adaptive compensating signals," *Control Eng. Pract.*, vol. 12, no. 3, pp. 283–290, Mar. 2004.
- [17] T. Song, B. Han, and S. Zhen, "Variable polarity LMS feedback based on displacement nulling to compensate unbalance of magnetic bearing," *J. Vib. Shock*, vol. 34, no. 7, pp. 24–32, Jul. 2015.
- [18] T. Schuhmann, W. Hofmann, and R. Werner, "Improving operational performance of active magnetic bearings using Kalman filter and state feedback control," *IEEE Trans. Ind. Electron.*, vol. 59, no. 2, pp. 821–829, Feb. 2012.
- [19] B. Han, Y. Liu, and S. Zhen, "Research on vibration suppression for magnetic suspension motor based on repetitive control method," *J. Vib. Meas. Diagnosis*, vol. 35, no. 3, pp. 486–492, Jun. 2015.
- [20] Y. Xu, H. Wu, and X. Guan, "Unbalance suppression for AMB rotor system using APF-SRF algorithm," *Shock Vib.*, vol. 2020, pp. 1–10, Jan. 2020.
- [21] Y. Maruyama, T. Mizuno, M. Takasaki, Y. Ishino, H. Kamenno, and A. Kubo, "Application of rotor unbalance compensation to an AMB-based gyroscopic sensor," *J. Syst. Des. Dyn.*, vol. 3, no. 4, pp. 572–583, 2009.
- [22] H. Zhu, Z. Yang, X. Sun, D. Wang, and X. Chen, "Rotor vibration control of a bearingless induction motor based on unbalanced force feed-forward compensation and current compensation," *IEEE Access*, vol. 8, pp. 12988–12998, 2020.
- [23] C. Zhang, "Three improved second order generalized integrators and the comparative analysis in phase locked loop application," *Trans. China Electrotech. Soc.*, vol. 32, no. 22, pp. 48–55, Nov. 2017.



**LI JI** was born in 1984. He received the Ph.D. degree in engineering from the Nanjing University of Aeronautics and Astronautics, Nanjing, China, in 2014.

From 2015 to 2020, he worked with the Postdoctoral Centre of State Grid Electric Power Research Institute. He is currently an Associate Professor at Hangzhou Dianzi University, China. His current research interest includes configuration and control method for high-speed magnetic suspension motors.



**XUEQING MA** was born in Shenyang, Liaoning, China, in 1996. She received the B.S. degree in automation from Hangzhou Dianzi University, China, and the M.S. degree in computer control and automation from Nanyang Technological University, Singapore, in 2020.

She was a Research Assistant with the Internet of Things (IoT) Laboratory and a Teaching Assistant of course EE4414 at Nanyang Technological University. She is currently an Assistant Professor at Hangzhou Dianzi University. Her research interests include power electronics, motor control, and deep learning neural networks.

• • •